

Article

# Luffa-like Interconnective Porous Nanofiber with Anchored Co/CoCr<sub>2</sub>O<sub>4</sub> Hybrid Nanoparticles for Zinc–Air Batteries

Guoqiang Jin <sup>1,†</sup>, Bin Liu <sup>2,\*</sup>, Yan Liu <sup>1,†</sup>, Xueting Zhang <sup>1</sup>, Dapeng Cao <sup>1,\*</sup> and Xiuling Zhang <sup>1,\*</sup><sup>1</sup> State Key Laboratory of Organic-Inorganic Composites, Beijing University of Chemical Technology, Beijing 100029, China; 2023210119@buct.edu.cn (G.J.); ly1307519@163.com (Y.L.); zxt1206yeah@163.com (X.Z.)<sup>2</sup> Beijing Mechanical Equipment Institute, Beijing 100039, China

\* Correspondence: lawrain1010@126.com (B.L.); caodp@mail.buct.edu.cn (D.C.); zxl3705@163.com (X.Z.)

† These authors contributed equally to this work.

## Abstract

The development of robust oxygen reduction reaction (ORR) catalyst with fast kinetics and good durability is significant for rechargeable zinc–air batteries (ZABs) but still remains a great challenge. Herein, inspired by the chain-like interconnective porous structure of plant luffa, an ORR catalyst of Co/CoCr<sub>2</sub>O<sub>4</sub>@IPCF is fabricated, with Co and CoCr<sub>2</sub>O<sub>4</sub> hybrid nanoparticles (NPs) embedding into interconnective porous carbon nanofibers (IPCF). Contributing to CoCr<sub>2</sub>O<sub>4</sub> NPs stabilized Co active sites, the resulting ZABs assembled with Co/CoCr<sub>2</sub>O<sub>4</sub>@IPCF as an air cathode catalyst delivering sustainable cycling stability of 550 h, surpassing that of Co@IPCF based on ZABs (215 h). Also, the Co/CoCr<sub>2</sub>O<sub>4</sub>@IPCF has a high ORR performance with a half-wave potential ( $E_{1/2}$ ) of 0.866 V in alkaline medium. The cycling stability originates from the IPCF carrier and the synergistic effect of Co NPs and CoCr<sub>2</sub>O<sub>4</sub> NPs. The chain-like interconnective porous structure of the fibers provides more active sites and facilitates mass transfer to avoid the accumulation of OH<sup>−</sup> and the exposure of H<sub>2</sub>O<sub>2</sub>, while the CoCr<sub>2</sub>O<sub>4</sub> NPs can serve as a regulator for stabilizing the Co NPs electrochemical performance.



Academic Editor: Hirotoshi Yamada

Received: 25 June 2025

Revised: 25 July 2025

Accepted: 7 August 2025

Published: 8 August 2025

**Citation:** Jin, G.; Liu, B.; Liu, Y.; Zhang, X.; Cao, D.; Zhang, X. Luffa-like Interconnective Porous Nanofiber with Anchored Co/CoCr<sub>2</sub>O<sub>4</sub> Hybrid Nanoparticles for Zinc–Air Batteries. *Batteries* **2025**, *11*, 306. <https://doi.org/10.3390/batteries11080306>

**Copyright:** © 2025 by the authors. Licensee MDPI, Basel, Switzerland. This article is an open access article distributed under the terms and conditions of the Creative Commons Attribution (CC BY) license (<https://creativecommons.org/licenses/by/4.0/>).

## 1. Introduction

Oxygen reduction reaction (ORR) is recognized as a key electrochemical reaction in zinc–air batteries (ZABs) as a potential energy device [1–3]. To date, the widely and effectively used ORR electrocatalysts are commercially available Pt-based catalysts [4–6]. However, the expensive cost and poor stability of Pt severely limit their wide applications in clean energy systems [7–10]. Therefore, the design and development of alternative catalysts with low cost and durability is imminent. Transition metal-based electrocatalysts [11–14] are gradually becoming substitutes for precious metals due to the characteristics of high efficiency and low cost. In order to rationally design transition metal electrocatalysts for ORR, it is necessary to regulate the electronic structure of the active center or optimize the geometry of the catalyst to facilitate the catalytic process [15–17]. Doping (SA-CoCu@Cu/CoNP, Sb-SeNC and phosphorus (P)-doped NiFe mixed oxides) [18–20], alloying (PtM (M = Fe, Ni)) [21–23], and introducing new phases (Co/Co<sub>3</sub>O<sub>4</sub>/CoF<sub>2</sub>@NSC and Co<sub>3</sub>O<sub>4</sub>/CeO<sub>2</sub> heterostructure) [24–26] to enhance their intrinsic catalytic activity are usually used to modulate the electronic properties of the active centers. Another solution is focused on

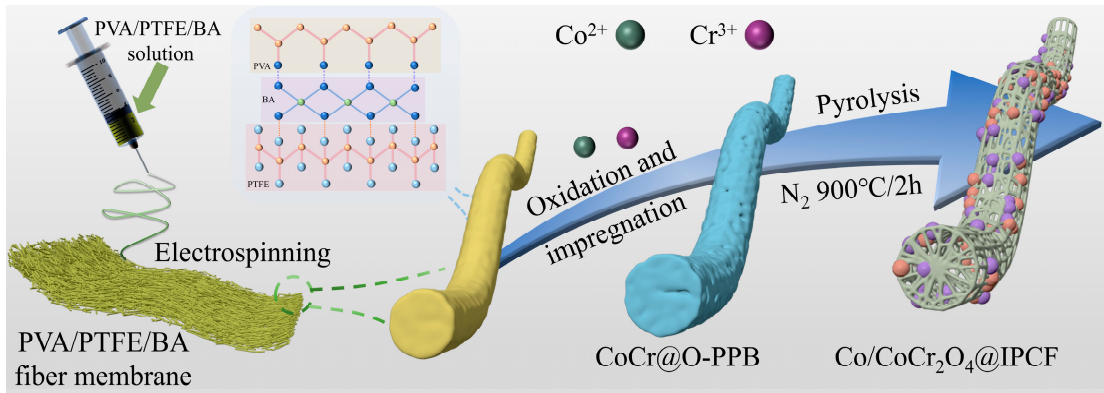
modulating the morphology and pore structure of the catalysts to increase the accessible surface area and ensure efficient mass transfer to active sites, thereby enhancing the catalytic activity [27–32]. For example, fiber structure of Zn/CoNC@CPCNFs and Co-N<sub>x</sub> nanocube/CNF [33,34], particular morphologies of cube Co(CN)<sub>3</sub>, and slices of NiFe-layered double hydroxide with Zn<sup>2+</sup>- or Al<sup>3+</sup>-decorated and hollow sea urchin-like Ag-Co<sub>3</sub>O<sub>4</sub> [35–37] were fabricated and used as the electrocatalysts. To solve the issues of deactivation and instability of cobalt, Chen et al. used ZrO<sub>2</sub> as the interface electron coupling to stabilize Co. Based on the concept, they synthesized hybrid nanoparticles of Co nanodots and ZrO<sub>2</sub> nanoparticles on porous carbon nanofibers. Importantly, they found that ZrO<sub>2</sub> also can act as an electron storage layer to store the electrons of Co and slowly release them to the interface, improving the stability of Co [38]. Additionally, Douka et al. combined interconnected microporous carbon matrix with cobalt–nitrogen–carbon active sites to enhance the electrochemical properties and durability of ZABs. The resultant silica-templated ZIF-67 assemblies exhibited superior ORR activity in terms of half-wave potential, limiting current density compared to the microporous carbon-loaded Co nanoparticle catalysts obtained by direct pyrolysis of ZIF-67 [39]. While a lot of attention has been paid to the combination of electronics modulation and porous carbon to improve the electrochemical performance, the most reported carbon matrix is not continuous and the pore structure is not interconnective. This makes it difficult to mass transfer fast and continuously, leading to the accumulation of OH<sup>−</sup> and the exposure of H<sub>2</sub>O<sub>2</sub>. Therefore, it remains a challenge to design and develop an efficient strategy that can combine multi-component electronic modulation with geometry optimization.

Inspired by interconnective porous luffa fiber structure, we propose a controllable strategy to prepare Co/CoCr<sub>2</sub>O<sub>4</sub>@IPCF catalysts by co-embedding Co and CoCr<sub>2</sub>O<sub>4</sub> hybrid NPs in chain-like interconnective porous carbon fiber (IPCF). The Co/CoCr<sub>2</sub>O<sub>4</sub>@IPCF exhibits a high half-wave potential ( $E_{1/2}$ ) of 0.866 V and an excellent stability of only a 7 mV decrease in  $E_{1/2}$  after 5000 CV cycles. When assembled into a liquid zinc-air battery as the air cathode catalyst, the Co/CoCr<sub>2</sub>O<sub>4</sub>@IPCF achieves a power density of 193.6 mW cm<sup>−2</sup> and long-term stability for 550 h. Those results can be ascribed to the fact that the chain-like interconnective porous carbon structure could promote mass transfer and expose more active sites, improving the ORR kinetics and further enhancing the intrinsic ORR activity. Importantly, the spinel phase CoCr<sub>2</sub>O<sub>4</sub> is favorable to stabilizing the Co active center and improving the durability of devices.

## 2. Results and Discussion

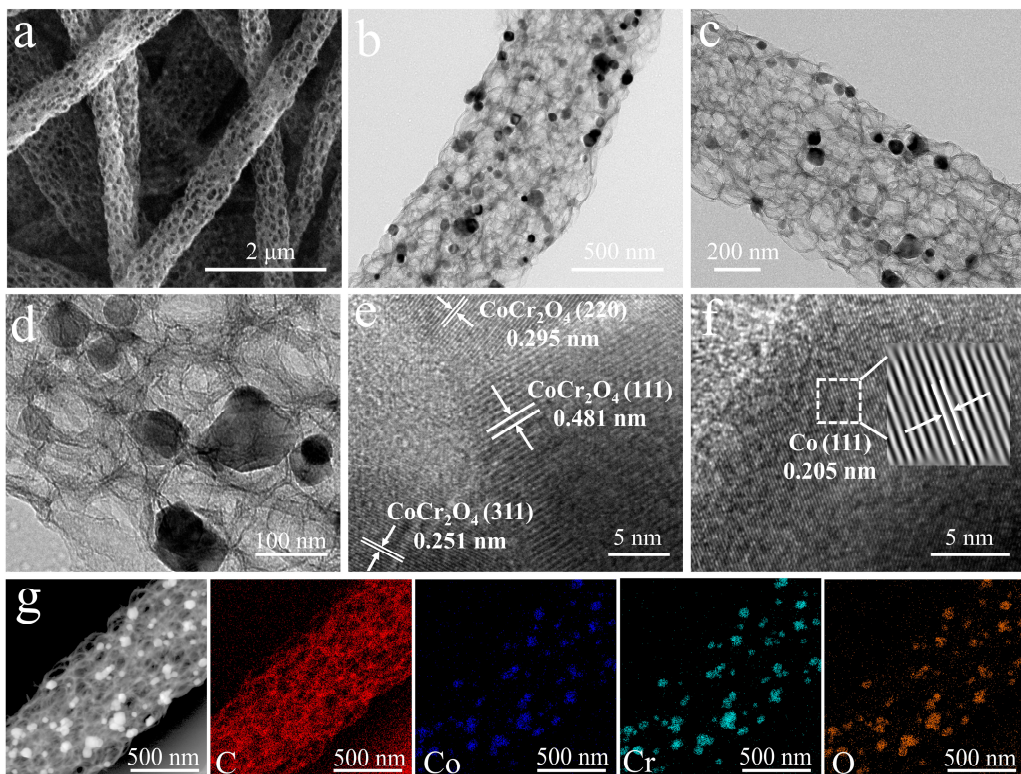
### 2.1. Preparation and Structural Characterization of Catalysts

Figure 1 shows a schematic diagram of the encapsulation of Co and CoCr<sub>2</sub>O<sub>4</sub> hybrid NPs in chain-like interconnective porous carbon fibers (IPCF) by electrostatic spinning, metal salt impregnation, and heat treatment. First, the PVA/PTFE/BA fiber membrane was prepared by electrospinning, in which PVA was easily hydrolyzed in BA solution, and PTFE would be rapidly cross-linked with PVA-BA to form a stable sol after adding PTFE emulsion to the PVA-BA solution [40,41]. O-PVA/PTFE/BA fibrous membranes were obtained by pre-oxidizing PVA/PTFE/BA fibrous membranes at 280 °C. The dehydrogenation reaction of PVA was accompanied by the formation of C=C conjugated bonds, which could improve the stability and continuity of the fibers. Then, the O-PVA/PTFE/BA fiber membrane was immersed in a methanol solution containing cobalt and chromium salts to achieve the impregnation of metal salts. Finally, Co/CoCr<sub>2</sub>O<sub>4</sub>@IPCF was produced by pyrolysis of PTFE during heat treatment to form chain-like interconnective porous fibers.



**Figure 1.** Schematic diagram of the formation process of Co/CoCr<sub>2</sub>O<sub>4</sub>@IPCF.

The morphologies of O-PVA/PTFE/BA, PCNF, Co@IPCF, and Co/CoCr<sub>2</sub>O<sub>4</sub>@IPCF were firstly observed by scanning electron microscopy (SEM) and transmission electron microscopy (TEM). The SEM images indicated all prepared samples of O-PPB, IPCF, Co@IPCF, and Co/CoCr<sub>2</sub>O<sub>4</sub>@IPCF totally had uniform fiber morphology (Figures S1a–d, S2a,b and 2a). The porous and continuous chain-like structure of IPCF, Co@IPCF, and Co/CoCr<sub>2</sub>O<sub>4</sub>@IPCF can be clearly seen from the SEM and TEM images (Figures S1d–f, S2b and 2a–c). The chain-like porous structure resulted from the decomposition of cross-linked structure of PTFE NPs and PVA during the carbonization process. The unique porous structure of the ultralong fiber helps to load nanoparticles and expose more active sites during the reaction process. After impregnation of Co salts and hybrid metal salts of Co and Cr, it was found that nanoparticles were anchored in interconnective porous carbon fibers network (Figures 2b–d and S2c). Compared with Co@IPCF, Co/CoCr<sub>2</sub>O<sub>4</sub>@IPCF remained a continuously ultralong fiber structure and a smaller size of NPs with 50–200 nm, which could be due to the high content of Co salt eroding the surface of the fibers. The composition of nanoparticles was confirmed by high-power transmission electron microscopy (HRTEM). The lattice fringes with spacings of 0.251, 0.295, and 0.481 nm were clearly observed in HRTEM images (Figure 2e), corresponding to the (311), (220), and (111) crystallographic planes of CoCr<sub>2</sub>O<sub>4</sub> (JCPDS 80-1668), respectively. Meanwhile, the lattice fringes with a pitch of 0.205 nm (Figure 2f) corresponded to the (111) planes of Co (JCPDS 15-0806). The results indicated the nanoparticles in Co/CoCr<sub>2</sub>O<sub>4</sub>@IPCF were composed of Co and CoCr<sub>2</sub>O<sub>4</sub> hybrids. The EDS mapping displayed the elemental distribution of Co/CoCr<sub>2</sub>O<sub>4</sub>@IPCF, with the C element uniformly distributed throughout the fibers, while the signals of Co, Cr, and O elements concentrated on the NPs (Figure 2g). In addition, inductively coupled plasma emission spectroscopy (ICP-OES, Table S1) also indicated the presence of Co and Cr elements with 28.819 wt% and 13.614 wt%, respectively. Meanwhile, the lattice spacing of NPs on Co@IPCF sample was determined to be 0.205 nm by HRTEM analysis (Figure S2d), ascribed to the (111) crystal plane of Co (JCPDS 15-0806), indicating that the NPs on Co@PCNF sample are Co NPs. Furthermore, the EDS presented that the C signal was uniformly distributed across the Co@IPCF, and Co signal was on the NPs (Figure S2e), further confirming that the Co NPs are anchored to the porous carbon fibers network.



**Figure 2.** (a) SEM images of Co/CoCr<sub>2</sub>O<sub>4</sub>@IPCF; (b–d) TEM images of Co/CoCr<sub>2</sub>O<sub>4</sub>@IPCF; (e,f) HRTEM images of Co/CoCr<sub>2</sub>O<sub>4</sub>@IPCF; (g) EDS images of Co/CoCr<sub>2</sub>O<sub>4</sub>@IPCF.

To further determine the composition of the samples, the XRD patterns of Co/CoCr<sub>2</sub>O<sub>4</sub>@IPCF were analyzed. In Figure 3a, Co/CoCr<sub>2</sub>O<sub>4</sub>@IPCF displayed diffraction peaks at 18.43°, 30.27°, and 35.63°, corresponding to the (111), (220), and (311) lattice planes of spinel-type CoCr<sub>2</sub>O<sub>4</sub> (PDF#80-1668), and the diffraction peak located at 44.2° was attributed to the (111) crystallographic plane of Co (PDF#15-0806) [42,43]. The XRD results are consistent with the HRTEM. The specific surface area (SSA) and pore size distribution of the samples were investigated by N<sub>2</sub> adsorption–desorption experiments. The N<sub>2</sub> adsorption curves increased sharply when  $p/p_0 < 0.1$  and  $> 0.9$  (Figure 3b), indicating that the samples all had a large number of pores. Moreover, the samples all exhibited type I/IV isotherms, and the type I and type IV isothermal properties indicated that the samples all had a graded porous structure [44–46], also verified in Figure S3. The SSA of Co/CoCr<sub>2</sub>O<sub>4</sub>@ICNF was 711.538 m<sup>2</sup> g<sup>-1</sup>, higher than that of Co@PCNF (374.632 m<sup>2</sup> g<sup>-1</sup>) but lower than that of PCNF (963.781 m<sup>2</sup> g<sup>-1</sup>). Based on the SEM images and pore size distribution curves of Co/CoCr<sub>2</sub>O<sub>4</sub>@IPCF and the comparison samples, it is inferred that the nanoparticles in Co/CoCr<sub>2</sub>O<sub>4</sub>@IPCF may clog some micropores and mesopores. The partial collapse of Co@IPCF fibers resulted in a lower SSA than Co/CoCr<sub>2</sub>O<sub>4</sub>@IPCF and IPCF. Figure S4 shows the TG-DSC curves of Co@IPCF and Co/CoCr<sub>2</sub>O<sub>4</sub>@IPCF, and the weight change can be attributed to three stages. The first stage can be attributed to the adsorption of water on the composites' surface before 100 °C, where the higher weight loss of Co/CoCr<sub>2</sub>O<sub>4</sub>@IPCF was due to its higher SSA than that of Co@IPCF. The second stage from 350 °C to 450 °C is mainly due to the absorption of oxygen by cobalt to form oxides, and after 450 °C, the mass loss of the two materials is all derived from the decomposition of IPCF. Therefore, it can be calculated that the carbon content of Co/CoCr<sub>2</sub>O<sub>4</sub>@IPCF and Co@IPCF is 13.1% and 42.54%, respectively. Figure S5 shows that the water contact angle was 13.68° of Co/CoCr<sub>2</sub>O<sub>4</sub>@IPCF, larger than that of IPCF (0°), illustrating the good wettability of both IPCF and Co/CoCr<sub>2</sub>O<sub>4</sub>@IPCF. The excellent wettability facilitates the

penetration and adsorption of the electrolyte on the electrode surface, which will facilitate mass transfer in hydrogen and oxygen evolution reactions. The intensity ratio ( $I_D/I_G$ ) of the D peak to the G peak is an important parameter reflecting the crystallinity of graphitic carbon in Raman spectroscopy, as shown in Figure 3c. The  $I_D/I_G$  values of Co/CoCr<sub>2</sub>O<sub>4</sub>@IPCF were higher than those of IPCF and Co@IPCF, indicating that the Co and CoCr<sub>2</sub>O<sub>4</sub> hybrid led to the increase in defects [47]. This is because during pyrolysis and carbonization, Co(NO<sub>3</sub>)<sub>2</sub>·6H<sub>2</sub>O and CrCl<sub>3</sub>·6H<sub>2</sub>O were reduced by carbon to form Co and CoCr<sub>2</sub>O<sub>4</sub> hybrid nanoparticles, leading to more defects in carbon. The existence of these defect sites is conducive to improving the catalytic performance of ORR in alkaline media [48].

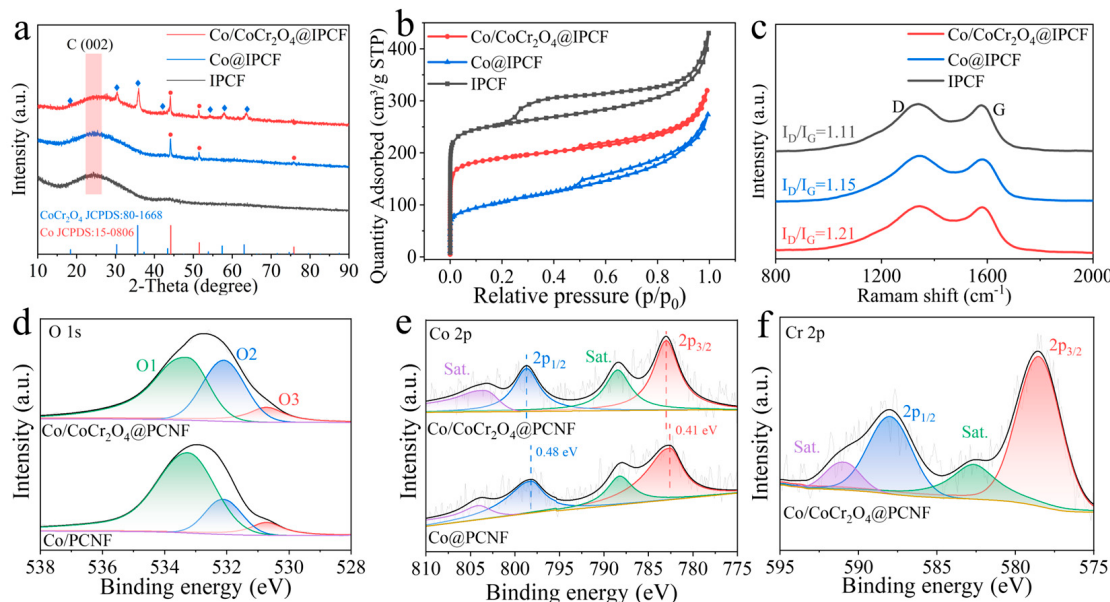


**Figure 3.** (a) XRD patterns of Co/CoCr<sub>2</sub>O<sub>4</sub>@IPCF, Co@IPCF, and IPCF; (b) N<sub>2</sub> adsorption–desorption isotherm; (c) Raman spectra; (d) high-resolution O 1s spectra of Co/CoCr<sub>2</sub>O<sub>4</sub>@IPCF and Co@IPCF; (e) high-resolution Co 2p spectra of Co/CoCr<sub>2</sub>O<sub>4</sub>@IPCF and Co@IPCF; (f) high-resolution Cr 2p spectra of Co/CoCr<sub>2</sub>O<sub>4</sub>@IPCF.

The surface elemental composition and chemical states of Co/CoCr<sub>2</sub>O<sub>4</sub>@IPCF and Co@IPCF were characterized by X-ray photoelectron spectroscopy (XPS). The XPS full spectrum analysis demonstrated the presence of elements C, Co, Cr, and O on the surface of the sample Co/CoCr<sub>2</sub>O<sub>4</sub>@IPCF (Figure S6), consistent with the EDS results. The O 1s XPS spectra of Co/CoCr<sub>2</sub>O<sub>4</sub>@IPCF and Co@IPCF show three peaks at 530.7 eV (O3), 532.1 eV (O2), and 533.26 eV (O1) (Figure 3d). The fitted O3 peak is associated with saturated lattice oxygen atoms with a coordination number of 3, the O2 peak may be associated with low-coordinated oxygen atoms with a coordination number of 2 or 1, and the O1 peak belongs to the O-H in the surface-adsorbed water molecules [49]. Compared to Co@IPCF, Co/CoCr<sub>2</sub>O<sub>4</sub>@IPCF had a higher concentration of low-coordinated surface oxygen atoms, illustrating the existence of oxides in Co/CoCr<sub>2</sub>O<sub>4</sub>@IPCF [50,51]. Furthermore, in view of Co 2p spectrum (Figure 3e), the binding energies of 782.59 eV and 798.21 eV correspond to Co 2p<sub>3/2</sub> and Co 2p<sub>1/2</sub>, respectively, while the peaks at 788.24 eV and 804.18 eV are attributed to the satellite peaks of Co 2p<sub>3/2</sub> and Co 2p<sub>1/2</sub>. Compared with Co@IPCF, the Co 2p<sub>3/2</sub> and Co 2p<sub>1/2</sub> peaks of Co/CoCr<sub>2</sub>O<sub>4</sub>@IPCF were shifted by 0.41 eV and 0.48 eV, respectively, suggesting the remodeling of the chemical coordination environments of Co species in Co/CoCr<sub>2</sub>O<sub>4</sub>@IPCF [52,53]. It can be mainly attributed to the strong electronic interactions formed between CoCr<sub>2</sub>O<sub>4</sub> NPs and Co NPs. The high-resolution Cr 2p

spectra can be deconvoluted into Cr 2p<sub>3/2</sub> (578.51 eV) and Cr 2p<sub>1/2</sub> (587.99 eV) and the corresponding satellite peaks (582.66 and 590.91 eV) (Figure 3f).

## 2.2. Electrocatalytic Activities of ORR and OER

In order to evaluate the ORR performance of Co/CoCr<sub>2</sub>O<sub>4</sub>@IPCF catalysts, electrochemical tests were performed using a rotating disk electrode (RDE) in O<sub>2</sub>-saturated 0.1 M KOH solution. First, the polarization curves of the samples were tested by linear scanning voltammetry (LSV). The half-wave potential ( $E_{1/2}$ ) of Co/CoCr<sub>2</sub>O<sub>4</sub>@IPCF was 0.866 V (Figure 4a), which was superior to that of Co@IPCF (0.86 V), PCNF (0.802 V), and Pt/C (0.85 V). And the limiting current ( $J_L$ ) of Co/CoCr<sub>2</sub>O<sub>4</sub>@IPCF was 6 mA cm<sup>-2</sup>, which was higher than that of Co@IPCF (5.05 mA cm<sup>-2</sup>) and PCNF (5.04 mA cm<sup>-2</sup>). Among them, the  $E_{1/2}$  of Co/CoCr<sub>2</sub>O<sub>4</sub>@IPCF and Co@IPCF were similar and much higher than that of IPCF. The result demonstrated that Co NPs had ORR activity in Co/CoCr<sub>2</sub>O<sub>4</sub>@IPCF, and the synergistic effect of Co NPs, CoCr<sub>2</sub>O<sub>4</sub> NPs, and IPCF contributed to the highest half-wave potentials and the largest limiting current density. Meanwhile, the dynamic current density ( $J_k$ ) of Co/CoCr<sub>2</sub>O<sub>4</sub>@IPCF at 0.85 V reached 10.2 mA cm<sup>-2</sup> (Figure 4b), much higher than that of Co@IPCF, Pt/C, and PCNF. Figure 4c shows the Tafel slopes of different catalysts. The Tafel slope of Co@IPCF is 62.78 mV dec<sup>-1</sup>, lower than that of PCNF (94.21 mV dec<sup>-1</sup>) and Pt/C (80.54 mV dec<sup>-1</sup>). In particular, the Tafel slope of Co/CoCr<sub>2</sub>O<sub>4</sub>@IPCF is 52.25 mV dec<sup>-1</sup>, superior to that of the noble metal Pt/C. The lower Tafel slope indicates that the Co/CoCr<sub>2</sub>O<sub>4</sub>@IPCF catalyst has good ORR kinetics. To quantitatively evaluate ECSA, the CV curves under different scanning rates (5–30 mV s<sup>-1</sup>) were tested (Figure S7), and the  $C_{dl}$  values were obtained by calculating the slope of the linear fitting of current density and scanning rate. In Figure 4d, the  $C_{dl}$  of Co/CoCr<sub>2</sub>O<sub>4</sub>@IPCF, Co@IPCF, and IPCF are 17.83, 12.2, and 6.6 mF cm<sup>-2</sup>, respectively, indicating that Co/CoCr<sub>2</sub>O<sub>4</sub>@IPCF has a larger ECSA. Therefore, electrochemical testing results suggested Co/CoCr<sub>2</sub>O<sub>4</sub>@IPCF can provide more active sites, effectively improving ORR performance [19,54].

The RRDE test results were able to calculate the number of electrons transferred ( $n$ ) and the H<sub>2</sub>O<sub>2</sub> yield in Co/CoCr<sub>2</sub>O<sub>4</sub>@IPCF. In the 0.2–0.8V range, the average  $n$  of Co/CoCr<sub>2</sub>O<sub>4</sub>@IPCF was 3.84 and the H<sub>2</sub>O<sub>2</sub> yield was less than 10% (Figure 4e), indicating that the Co/CoCr<sub>2</sub>O<sub>4</sub>@IPCF catalyst mainly followed the four-electron reaction path in the ORR catalytic process. The results of the methanol tolerance test are presented in Figure 4f. It can be seen that the current density of Pt/C was greatly reduced after the addition of methanol (about 40% drop) and could not be recovered after 600 s, which showed the typical phenomenon of methanol poisoning. In contrast, the current density of Co/CoCr<sub>2</sub>O<sub>4</sub>@IPCF showed only a small change (<5% change) after the addition of methanol, indicating that Co/CoCr<sub>2</sub>O<sub>4</sub>@IPCF has a high methanol tolerance. To evaluate the stability of the Co/CoCr<sub>2</sub>O<sub>4</sub>@IPCF catalyst, accelerated durability testing (ADT) was performed in the potential interval of 0.6–0.95 V vs. RHE. As illustrated in Figure 4g, the  $E_{1/2}$  of the catalyst decayed by only 7 mV after 5000 turns of cyclic voltammetry (CV) test for Co/CoCr<sub>2</sub>O<sub>4</sub>@IPCF. Furthermore, at a constant potential of 0.41 V vs. RHE, after 100 h of testing, the current retention rate of Co/CoCr<sub>2</sub>O<sub>4</sub>@IPCF was 90.6% (Figure 4h), which was significantly better than that of Co@IPCF (16.5 h, 70.3%), IPCF (20 h, 70.4%), and Pt/C (14.1 h, 85.6%). The significant performance differences between Co/CoCr<sub>2</sub>O<sub>4</sub>@IPCF and Co@IPCF demonstrate that the introduction of spinel phase CoCr<sub>2</sub>O<sub>4</sub> is crucial for stabilizing the Co active center.

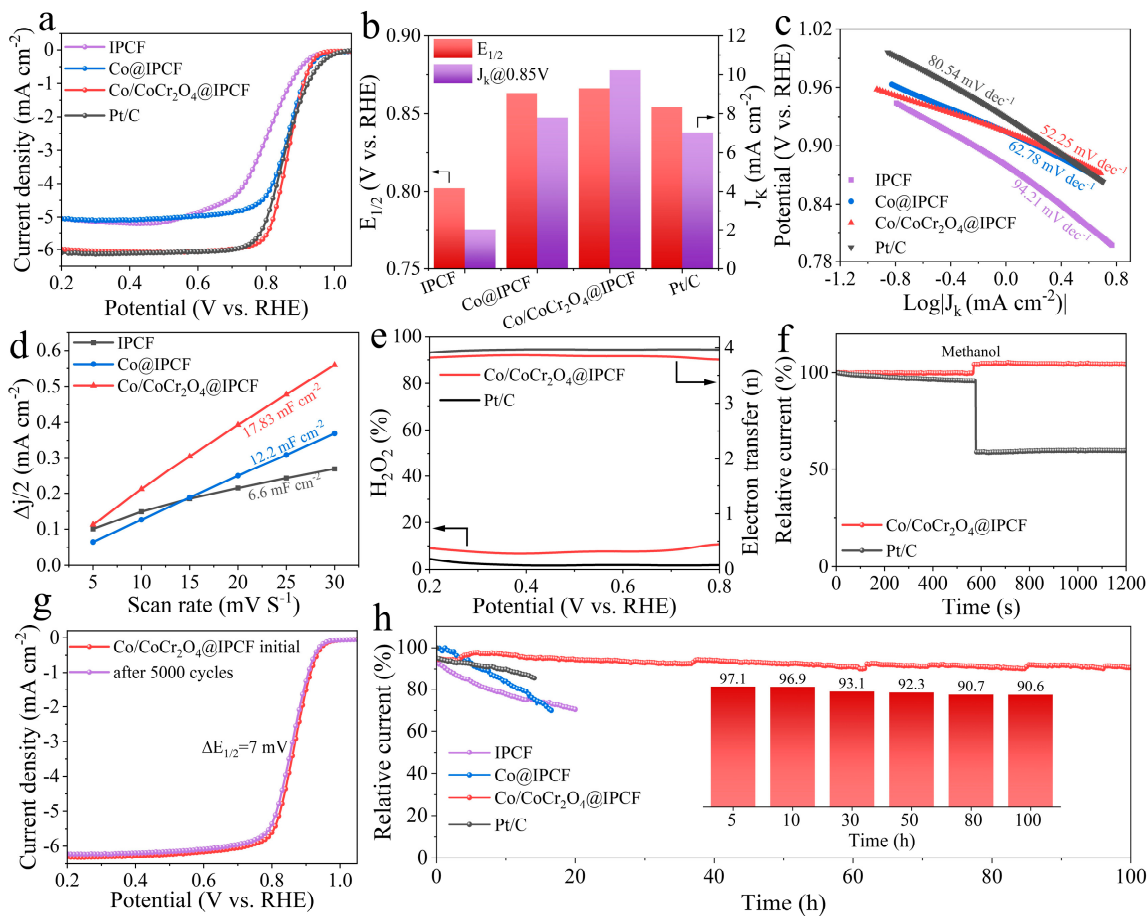


**Figure 4.** (a) LSV curves; (b) comparison plots of  $E_{1/2}$  and  $J_k$ ; (c) the corresponding Tafel curves for the samples; (d) the fitting of double-layer capacitances; (e) number of transferred electrons and  $H_2O_2$  yield; (f) methanol resistance tests; (g) LSV curves of  $Co/CoCr_2O_4@IPCF$  catalyst before and after CV cycle; (h) current normalized chronocurrent curves at 0.41 V vs. RHE.

The electrochemical performance data of  $Co/CoCr_2O_4@IPCF$  and reference samples are presented in Figure S8 and Table S2. A comprehensive analysis reveals that the  $Co/CoCr_2O_4@IPCF$  catalyst exhibits outstanding advantages in both activity and stability. The remarkable catalytic activity of  $Co/CoCr_2O_4@IPCF$  is primarily attributed to the synergistic effect between  $CoCr_2O_4$  NPs and Co NPs, as well as the supporting role of PCNF. The high half-wave potential of  $Co@IPCF$  indicated that Co NPs possess high intrinsic activity. The enhancement performance of the kinetic current density and the Tafel slope in  $Co/CoCr_2O_4@IPCF$  can be ascribed to the synergy between  $CoCr_2O_4$  NPs and Co NPs for accelerating charge transfer, thereby improving the kinetics of the ORR. The PCNF support endows  $Co/CoCr_2O_4@IPCF$  with a high specific surface area ( $711.538\text{ m}^2\text{ g}^{-1}$ ) and a unique chain-like porous structure. This porous fiber architecture enhances mass transport at the reaction interface, enabling the loaded  $Co/CoCr_2O_4$  NPs to exhibit exceptional ORR activity. The long-term stability of  $Co/CoCr_2O_4@IPCF$  is mainly attributed to the strong interaction between Co NPs and  $CoCr_2O_4$  NPs. The  $Co/CoCr_2O_4@IPCF$  shows far superior stability compared to  $Co@IPCF$  and IPCF. It can be possible that the  $CoCr_2O_4$  NPs are favorable to forming a strong electron-coupled interface with Co NPs, then stabilizing the dispersed Co NPs and achieving excellent durability [38]. Therefore,  $Co/CoCr_2O_4@IPCF$  combines exceptional catalytic activity with long-term stability, making it a highly efficient ORR catalyst.

Based on the above experimental results, the possible mechanism of the unique structure of  $Co/CoCr_2O_4@IPCF$  for the enhancement of its ORR activity is described in

**Figure 5.** The large surface area and chain-like porous structure of Co/CoCr<sub>2</sub>O<sub>4</sub>@IPCF optimized the local interfacial environment of the catalyst, making it more suitable for ORR. Specifically, the interconnective chain-like porous structure provided abundant and continuous channels for O<sub>2</sub> transport, which not only enhanced the O<sub>2</sub> diffusion rate but also enhanced the O<sub>2</sub> concentration at the three-phase reaction interface, thus improving the ORR kinetics. Meanwhile, the chain-like porous structure also provided abundant interfaces for the contact between the active sites and electrolyte/electrons, which further enhanced the overall activity of the catalyst. In contrast, in catalysts lacking a chain-like porous structure, it is difficult for O<sub>2</sub> to diffuse rapidly through the pores to each active site, resulting in a limited reaction efficiency. Therefore, encapsulation of NPs in fibers with an interconnective chain-like porous structure is an effective strategy for the preparation of electrocatalysts.

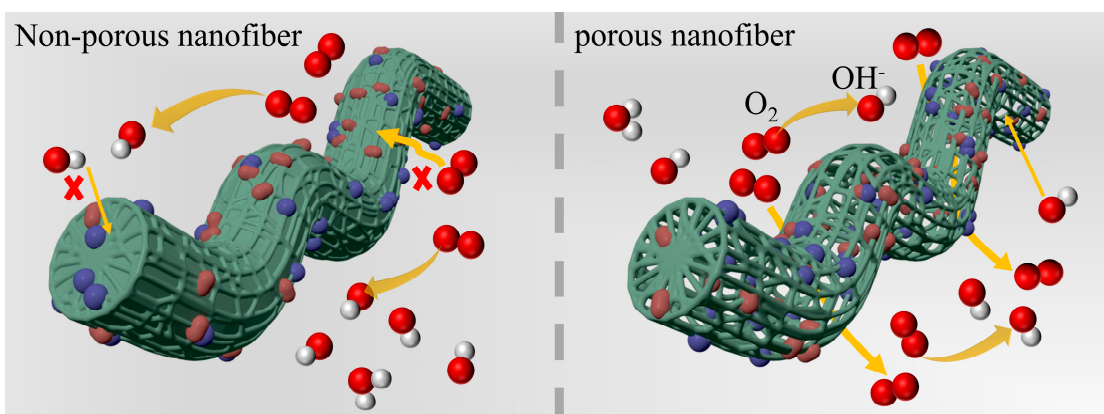


**Figure 5.** Schematic comparison of the ORR mechanism of nonporous fibers and chained porous fibers.

### 2.3. Performance of Zinc–Air Batteries

Given the excellent ORR catalytic performance of Co/CoCr<sub>2</sub>O<sub>4</sub>@IPCF, this was further used as a cathode catalyst for liquid ZABs to evaluate its potential in practical applications (Figure 6a). For comparison, Pt/C (20 wt%) was also tested under the same conditions. Constant current discharge measurements (Figure 6b) show that a ZAB with Co/CoCr<sub>2</sub>O<sub>4</sub>@IPCF shows an open-circuit voltage of 1.469 V, slightly higher than that of Pt/C (1.456 V). As shown in Figure 6c, the peak power density of Co/CoCr<sub>2</sub>O<sub>4</sub>@IPCF-based ZABs is 193.6 mW cm<sup>-2</sup>, while the peak power density of Pt/C-based ZABs is 158.9 mW cm<sup>-2</sup>. At a constant current density of 10 mA cm<sup>-2</sup>, the Co/CoCr<sub>2</sub>O<sub>4</sub>@IPCF-based ZAB provides a specific capacity of 810.6 mAh gZn<sup>-1</sup> (Figure 6d), surpassing the Pt/C-based ZAB (759.25 mAh gZn<sup>-1</sup>). In addition, the stability of the Co/CoCr<sub>2</sub>O<sub>4</sub>@IPCF-based ZAB at different current densities was tested. The Co/CoCr<sub>2</sub>O<sub>4</sub>@IPCF-based ZAB was able to operate stably for 24 h at different current densities of 5 mA cm<sup>-2</sup>, 10 mA cm<sup>-2</sup>, 20 mA cm<sup>-2</sup>, and 30 mA cm<sup>-2</sup> (Figure 6e), and the voltage of the Co/CoCr<sub>2</sub>O<sub>4</sub>@IPCF-based ZAB decreased slightly from 1.296 V to 1.272 V at 10 mA cm<sup>-2</sup> (with an attenuation rate of only 1.85%). To further evaluate the stability of the Co/CoCr<sub>2</sub>O<sub>4</sub>@IPCF catalyst in ZAB applications, a mixed air electrode was prepared by mixing Co/CoCr<sub>2</sub>O<sub>4</sub>@IPCF with RuO<sub>2</sub> (ZAB based on Co/CoCr<sub>2</sub>O<sub>4</sub>@IPCF + RuO<sub>2</sub>) and the according ZAB was subjected to a charge–discharge cycle test at 5 mA cm<sup>-2</sup>. As shown in Figure 6f, charge–discharge voltages of the battery are relatively stable above 540 h, and the round-trip efficiency decreases from the initial 60.9% to 56.5% (with only a decrease of 4.4%). However, the durability of Co@IPCF+RuO<sub>2</sub>-based ZABs and Pt/C+RuO<sub>2</sub>-based ZABs was poor at 215 h and 210 h, respectively. In conclusion, the introduction of CoCr<sub>2</sub>O<sub>4</sub> NPs can improve the stability of

the Co active site, thereby enhancing the cycling stability of ZABs. In addition, we compare Co/CoCr<sub>2</sub>O<sub>4</sub>@IPCF with other reported electrocatalysts, which shows that the prepared catalysts have excellent performance (Table S3).

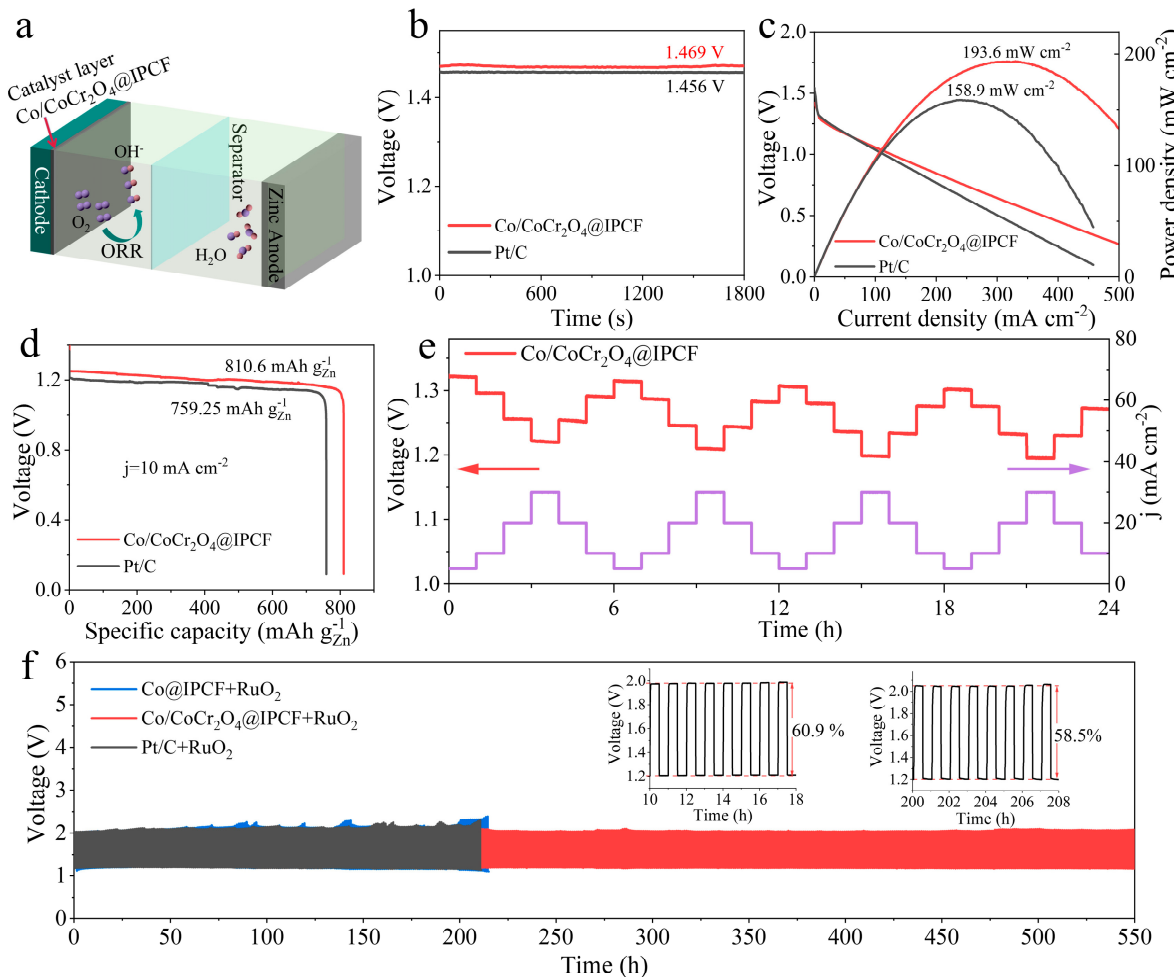


**Figure 6.** (a) Schematic diagram of a zinc–air battery; (b) open-circuit voltages; (c) discharge polarization curves and power densities; (d) specific capacities; (e) discharge stability of Co/CoCr<sub>2</sub>O<sub>4</sub>@IPCF-based ZABs at different current densities; (f) long-time charge/discharge cycling stability at 5 mA cm<sup>-2</sup> (the inset shows the corresponding voltage efficiency plots during cycling).

### 3. Conclusions

In summary, we successfully embedded Co and CoCr<sub>2</sub>O<sub>4</sub> hybrid nanoparticles into chain-like interconnective porous nanofibers through electrospinning, impregnation, and thermal treatment. Electrochemical tests demonstrated that Co/CoCr<sub>2</sub>O<sub>4</sub>@IPCF exhibited a high half-wave potential of 0.866 V along with good catalytic stability. More importantly, the ZAB assembled with the Co/CoCr<sub>2</sub>O<sub>4</sub>@IPCF catalyst showed remarkable electrochemical performance, achieving not only a high peak power density of 193.6 mW cm<sup>-2</sup> but also good cycling stability during 550 h of continuous charge–discharge testing. Combined structural characterization and performance analysis revealed that the superior ORR activity of the Co/CoCr<sub>2</sub>O<sub>4</sub>@IPCF catalyst stems from the synergistic effect between Co and CoCr<sub>2</sub>O<sub>4</sub> components as well as the supporting role of the continuous porous fiber structure. The unique porous architecture ensures rapid charge transfer and exposes more active sites, thereby enhancing ORR catalytic activity. Significantly, we found that the CoCr<sub>2</sub>O<sub>4</sub> nanoparticles can be used as a stabilizer to enhance the stability of active sites.

This work presents a simple yet effective strategy to improve both the ORR activity and stability of transition metal composites in alkaline solutions.

**Supplementary Materials:** The following supporting information can be downloaded at: <https://www.mdpi.com/article/10.3390/batteries11080306/s1>, Figure S1: (a,b) SEM images of O-PVA/PTFE/BA; (c,d) SEM images of IPCF; (e,f) TEM images of IPCF; Figure S2: (a,b) SEM image of Co@IPCF; (c) TEM image of Co@IPCF; (d) HRTEM image of Co@IPCF; (e) EDS images of Co@IPCF; Figure S3: Pore width distribution; Figure S4: TG-DSC curves for Co/CoCr<sub>2</sub>O<sub>4</sub>@IPCF and Co@IPCF; Figure S5: Water contact angle measurement of Co/CoCr<sub>2</sub>O<sub>4</sub>@IPCF (a) and IPCF (b); Figure S6: XPS survey spectrum of Co/CoCr<sub>2</sub>O<sub>4</sub>@IPCF and Co@IPCF; Figure S7: (a–c) CV curves of IPCF, Co @IPCF, and Co/CoCr<sub>2</sub>O<sub>4</sub>@IPCF in the non-Faraday interval at scanning rates from 5 to 30 mV s<sup>-1</sup>; Figure S8: Performance comparison of Co/CoCr<sub>2</sub>O<sub>4</sub>@IPCF with comparison samples; Table S1: Co and Cr content in Co/CoCr<sub>2</sub>O<sub>4</sub>@IPCF by ICP-OES test; Table S2: Performance comparison of Co/CoCr<sub>2</sub>O<sub>4</sub>@IPCF with comparison samples; Table S3: Comparison of properties of Co/CoCr<sub>2</sub>O<sub>4</sub>@IPCF with other catalysts reported in the literature. References [55–75] are cited in the Supplementary Materials.

**Author Contributions:** Conceptualization, G.J.; methodology, Y.L.; validation, X.Z. (Xueting Zhang); investigation, G.J. and Y.L.; resources, G.J., Y.L., and B.L.; data curation, G.J.; writing—original draft preparation, Y.L.; writing—review and editing, B.L., X.Z. (Xiuling Zhang), and D.C.; supervision, X.Z. (Xiuling Zhang) and D.C.; project administration, X.Z. (Xiuling Zhang); funding acquisition, X.Z. (Xiuling Zhang). All authors have read and agreed to the published version of the manuscript.

**Funding:** This research was funded by the National Natural Science Foundation of China (No 52103250), and the Fundamental Research Funds for the Central Universities (buctrc202213).

**Data Availability Statement:** The original contributions presented in this study are included in the article/Supplementary Materials. Further inquiries can be directed to the corresponding authors.

**Conflicts of Interest:** The authors declare no conflicts of interest.

## References

- Li, W.; Liu, B.; Liu, D.; Guo, P.F.; Liu, J.; Wang, R.R.; Guo, Y.H.; Tu, X.; Pan, H.G.; Sun, D.L.; et al. Alloying Co Species into Ordered and Interconnected Macroporous Carbon Polyhedra for Efficient Oxygen Reduction Reaction in Rechargeable Zinc-Air Batteries. *Adv. Mater.* **2022**, *34*, 2109605. [[CrossRef](#)] [[PubMed](#)]
- Zhang, X.; Zhu, X.; Liu, X.; Alwarappan, S. Transformation of Biomass Precursor into Both High-Efficiency Cathode Catalyst and Solid Electrolyte for Rechargeable Zn-Air Batteries. *Small* **2025**, *2502395*. [[CrossRef](#)] [[PubMed](#)]
- González-Morales, J.; Mosa, J.; Aparicio, M. Binder-Free Fe-N-C-O Bifunctional Electrocatalyst in Nickel Foam for Aqueous Zinc–Air Batteries. *Batteries* **2025**, *11*, 159. [[CrossRef](#)]
- Liu, H.B.; Xie, R.X.; Niu, Z.Q.; Jia, Q.H.; Yang, L.; Wang, S.T.; Cao, D.P. Two-in-one strategy to construct bifunctional oxygen electrocatalysts for rechargeable Zn-air battery. *Chin. J. Catal.* **2022**, *43*, 2906–2912. [[CrossRef](#)]
- Wang, Z.; Lu, Z.; Ye, Q.T.; Yang, Z.B.; Xu, R.J.; Kong, K.X.; Zhang, Y.F.; Yan, T.; Liu, Y.P.; Pan, Z.J.; et al. Construction of Fe Nanoclusters/Nanoparticles to Engineer FeN<sub>4</sub> Sites on Multichannel Porous Carbon Fibers for Boosting Oxygen Reduction Reaction. *Adv. Funct. Mater.* **2024**, *34*, 2315150. [[CrossRef](#)]
- Arif, M.; Mahsud, A.; Muhsin, T.; Deepak, F.L. Design, synthesis, and electronic structure modulation of ORR electrocatalysts. *J. Environ. Chem. Eng.* **2024**, *12*, 113417. [[CrossRef](#)]
- Qin, J.Y.; Liu, H.; Zou, P.C.; Zhang, R.; Wang, C.Y.; Xin, H.L. Altering Ligand Fields in Single-Atom Sites through Second-Shell Anion Modulation Boosts the Oxygen Reduction Reaction. *J. Am. Chem. Soc.* **2022**, *144*, 2197–2207. [[CrossRef](#)]
- Li, Z.J.; Ji, S.Q.; Wang, C.; Liu, H.X.; Leng, L.P.; Du, L.; Gao, J.C.; Qiao, M.; Horton, J.H.; Wang, Y. Geometric and Electronic Engineering of Atomically Dispersed Copper-Cobalt Diatomic Sites for Synergistic Promotion of Bifunctional Oxygen Electrocatalysis in Zinc-Air Batteries. *Adv. Mater.* **2023**, *35*, 2300905. [[CrossRef](#)]
- Chong, L.; Wen, J.G.; Kubal, J.; Sen, F.G.; Zou, J.X.; Greeley, J.; Chan, M.; Barkholtz, H.; Ding, W.J.; Liu, D.J. Ultralow-loading platinum-cobalt fuel cell catalysts derived from imidazolate frameworks. *Science* **2018**, *362*, 1276–1281. [[CrossRef](#)]
- Yang, G.G.; Zhu, J.W.; Yuan, P.F.; Hu, Y.F.; Qu, G.; Lu, B.A.; Xue, X.Y.; Yin, H.B.; Cheng, W.Z.; Cheng, J.Q.; et al. Regulating Fe-spin state by atomically dispersed Mn-N in Fe-N-C catalysts with high oxygen reduction activity. *Nat. Commun.* **2021**, *12*, 1734. [[CrossRef](#)]

11. Yan, J.H.; Dong, K.Q.; Zhang, Y.Y.; Wang, X.; Aboalhassan, A.A.; Yu, J.Y.; Ding, B. Multifunctional flexible membranes from sponge-like porous carbon nanofibers with high conductivity. *Nat. Commun.* **2019**, *10*, 5584. [[CrossRef](#)] [[PubMed](#)]
12. Ma, Y.; Xiao, Y.H.; Ge, Y.F.; Gao, D.G.; Zhang, Y.G.; Li, Z.P.; Han, Y.D. Constructing Fe-N-doped porous carbon nanofibers for a pH-universal ORR and switchable, superior Zn-air batteries. *J. Mater. Chem. A* **2024**, *12*, 2004–2010. [[CrossRef](#)]
13. Cheng, Q.Q.; Yang, L.J.; Zou, L.L.; Zou, Z.Q.; Chen, C.; Hu, Z.; Yang, H. Single Cobalt Atom and N Codoped Carbon Nanofibers as Highly Durable Electrocatalyst for Oxygen Reduction Reaction. *ACS Catal.* **2017**, *7*, 6864–6871. [[CrossRef](#)]
14. Bai, Q.; Shen, F.C.; Li, S.L.; Liu, J.; Dong, L.Z.; Wang, Z.M.; Lan, Y.Q. Cobalt@Nitrogen-Doped Porous Carbon Fiber Derived from the Electrospun Fiber of Bimetal-Organic Framework for Highly Active Oxygen Reduction. *Small Methods* **2018**, *2*, 1800049. [[CrossRef](#)]
15. Han, Z.L.; Chai, S.Y.; Zhu, Y.Q.; Yao, X.Y.; Yang, L.F.; Du, C.L.; Ma, X.L.; Cao, C.B.; Zou, M.S. Pre-coordination anchoring strategy for modulating the coordination structure of iron single atoms and ORR performance. *Chem. Eng. J.* **2024**, *502*, 157943. [[CrossRef](#)]
16. Liu, M.L.; Zhao, Z.P.; Duan, X.F.; Huang, Y. Nanoscale Structure Design for High-Performance Pt-Based ORR Catalysts. *Adv. Mater.* **2019**, *31*, 1802234. [[CrossRef](#)]
17. Zhang, X.; Gong, Y.; Li, S.; Sun, C. Porous Perovskite  $\text{La}_{0.6}\text{Sr}_{0.4}\text{Co}_{0.8}\text{Mn}_{0.2}\text{O}_3$  Nanofibers Loaded with  $\text{RuO}_2$  Nanosheets as an Efficient and Durable Bifunctional Catalyst for Rechargeable  $\text{Li}-\text{O}_2$  Batteries. *ACS Catal.* **2017**, *7*, 7737–7747. [[CrossRef](#)]
18. Zhang, Q.R.; Kumar, P.; Zhu, X.F.; Daiyan, R.; Bedford, N.M.; Wu, K.H.; Han, Z.J.; Zhang, T.R.; Amal, R.; Lu, X.Y. Electronically Modified Atomic Sites Within a Multicomponent Co/Cu Composite for Efficient Oxygen Electroreduction. *Adv. Energy Mater.* **2021**, *11*, 2100303. [[CrossRef](#)]
19. Niu, Z.Q.; Lu, Z.K.; Qiao, Z.L.; Xing, M.H.; Han, L.K.; Wang, S.T.; Cao, D.P. Long-Range Regulation of Se Doping for Oxygen Reduction of Atomically Dispersed Sb Catalysts for Ultralow-Temperature Solid-State Zn-Air Batteries. *ACS Catal.* **2023**, *13*, 7122–7131. [[CrossRef](#)]
20. Li, X.; Deng, C.; Kong, Y.; Huo, Q.; Mi, L.; Sun, J.; Cao, J.; Shao, J.; Chen, X.; Zhou, W.; et al. Unlocking the Transition of Electrochemical Water Oxidation Mechanism Induced by Heteroatom Doping. *Angew. Chem. Int. Ed.* **2023**, *62*, e202309732. [[CrossRef](#)]
21. Zhou, Z.; Zhang, H.-J.; Feng, X.; Ma, Z.; Ma, Z.-F.; Xue, Y. Progress of Pt and iron-group transition metal alloy catalysts with high ORR activity for PEMFCs. *J. Electroanal. Chem.* **2024**, *959*, 118165. [[CrossRef](#)]
22. Garapati, M.S.; Sundara, R. Highly efficient and ORR active platinum-scandium alloy-partially exfoliated carbon nanotubes electrocatalyst for Proton Exchange Membrane Fuel Cell. *Int. J. Hydrogen Energy* **2019**, *44*, 10951–10963. [[CrossRef](#)]
23. Liu, H.J.; Sun, F.M.; Yang, L.; Chen, M.; Wang, H.J. Gaining insight into the impact of electronic property and interface electrostatic field on ORR kinetics in alloy engineering via theoretical prognostication and experimental validation. *Colloid Interface Sci.* **2023**, *652*, 890–900. [[CrossRef](#)] [[PubMed](#)]
24. Li, H.; Yan, G.L.; Zhao, H.Y.; Howlett, P.C.; Wang, X.A.; Fang, J. Earthworm-Inspired Co/Co<sub>3</sub>O<sub>4</sub>/CoF<sub>2</sub>@NSC Nanofibrous Electrocatalyst with Confined Channels for Enhanced ORR/OER Performance. *Adv. Mater.* **2024**, *36*, 2311272. [[CrossRef](#)] [[PubMed](#)]
25. Guo, S.Q.; Wang, J.A.; Sun, Y.X.; Peng, L.C.; Li, C.J. Interface engineering of Co<sub>3</sub>O<sub>4</sub>/CeO<sub>2</sub> heterostructure in-situ embedded in Co/N-doped carbon nanofibers integrating oxygen vacancies as effective oxygen cathode catalyst for Li-O<sub>2</sub> battery. *Chem. Eng. J.* **2023**, *452*, 139317. [[CrossRef](#)]
26. Zhao, J.-W.; Wang, H.-Y.; Feng, L.; Zhu, J.-Z.; Liu, J.-X.; Li, W.-X. Crystal-Phase Engineering in Heterogeneous Catalysis. *Chem. Rev.* **2024**, *124*, 164–209. [[CrossRef](#)]
27. Chen, X.; Pu, J.; Hu, X.H.; Yao, Y.C.; Dou, Y.B.; Jiang, J.J.; Zhang, W.J. Janus Hollow Nanofiber with Bifunctional Oxygen Electrocatalyst for Rechargeable Zn-Air Battery. *Small* **2022**, *18*, 2200578. [[CrossRef](#)]
28. Wang, G.; Gao, H.J.; Yan, Z.R.; Li, L.; Li, Q.X.; Fan, J.; Zhao, Y.X.; Deng, N.P.; Kang, W.M.; Cheng, B.W. Copper nanodot-embedded nitrogen and fluorine co-doped porous carbon nanofibers as advanced electrocatalysts for rechargeable zinc-air batteries. *Colloid Interface Sci.* **2023**, *647*, 163–173. [[CrossRef](#)]
29. Zhang, L.L.; Liu, Y.Y.; Liu, S.L.; Zhou, L.M.; Wu, X.L.; Guo, X.J.; Zhang, A.Q.; Zhang, P.X.; Li, B.J.; Jiang, J.C. Mn-doped Co nanoparticles on wood-derived monolithic carbon for rechargeable zinc-air batteries. *J. Mater. Chem. A* **2023**, *11*, 22951–22959. [[CrossRef](#)]
30. Wu, L.; Zhao, R.; Du, G.; Wang, H.; Hou, M.; Zhang, W.; Sun, P.; Chen, T. Hierarchically porous Fe/N/S/C nanospheres with high-content of Fe-N<sub>x</sub> for enhanced ORR and Zn-air battery performance. *Green Energy Environ.* **2023**, *8*, 1693–1702. [[CrossRef](#)]
31. Sun, Z.; Guo, C.; Wang, F. Effect of Porous and Highly N,O-Doped Amorphous Carbon Materials with Defects Generated by KOH Etching on the Stability of ORR Catalysts. *Energy Fuels* **2024**, *38*, 18010–18017. [[CrossRef](#)]
32. Zhu, G.; Zhu, W.; Lou, Y.; Ma, J.; Yao, W.; Zong, R.; Zhu, Y. Encapsulate  $\alpha$ -MnO<sub>2</sub> nanofiber within graphene layer to tune surface electronic structure for efficient ozone decomposition. *Nat. Commun.* **2021**, *12*, 4152. [[CrossRef](#)] [[PubMed](#)]
33. Peng, L.; Sun, Y.; Guo, S.; Li, C. Highly efficient construction of hollow Co-N<sub>x</sub> nanocube cage dispersion implanted with porous carbonized nanofibers for Li-O<sub>2</sub> batteries. *J. Mater. Chem. A* **2022**, *10*, 740–751. [[CrossRef](#)]

34. Peng, L.; Zhang, X.; Sun, Y.; Li, C. Electrospun ZIF-derived cavity porous carbon nanofibers as a freestanding cathode for lithium–oxygen batteries with ultralow overpotential. *Nanoscale* **2021**, *13*, 16477–16486. [CrossRef] [PubMed]
35. Sun, K.; Dong, J.; Sun, H.; Wang, X.; Fang, J.; Zhuang, Z.; Tian, S.; Sun, X. Co(CN)<sub>3</sub> catalysts with well-defined coordination structure for the oxygen reduction reaction. *Nat. Catal.* **2023**, *6*, 1164–1173. [CrossRef]
36. Xie, Q.; Cai, Z.; Li, P.; Zhou, D.; Bi, Y.; Xiong, X.; Hu, E.; Li, Y.; Kuang, Y.; Sun, X. Layered double hydroxides with atomic-scale defects for superior electrocatalysis. *Nano Res.* **2018**, *11*, 4524–4534. [CrossRef]
37. Wang, Y.; Miao, L.; Shi, R.; Lu, M.; Wang, P. Unraveling the Synergistic Effect of Hollow Sea Urchin-like Ag-Co<sub>3</sub>O<sub>4</sub> Heterostructures in Electrochemical Dehydrogenation Reactions: Interface-Enhanced Electron Transfer and Desorption Process. *ACS Catal.* **2025**, *15*, 7966–7978. [CrossRef]
38. Chen, S.; Ma, Y.Y.; Zhang, L.; Zhang, Y.Y.; Chen, Y.H.; Zhang, X.H.; Yan, J.H. The Contact Interface Electronic Coupling of Cobalt and Zirconia Enables Stable and Highly Efficient 4e<sup>-</sup> Oxygen Reduction Reaction Catalysis. *Small* **2024**, *20*, 2307278. [CrossRef]
39. Douka, A.I.; Xu, Y.Y.; Yang, H.; Zaman, S.; Yan, Y.; Liu, H.F.; Salam, M.A.; Xia, B.Y. A Zeolitic-Imidazole Frameworks-Derived Interconnected Macroporous Carbon Matrix for Efficient Oxygen Electrocatalysis in Rechargeable Zinc-Air Batteries. *Adv. Mater.* **2020**, *32*, 2002170. [CrossRef]
40. Lu, B.L.; Lin, F.C.; Jiang, X.; Cheng, J.J.; Lu, Q.L.; Song, J.B.; Chen, C.; Huang, B. One-Pot Assembly of Microfibrillated Cellulose Reinforced PVA-Borax Hydrogels with Self-Healing and pH-Responsive Properties. *ACS Sustain. Chem. Eng.* **2017**, *5*, 948–956. [CrossRef]
41. Wang, Z.K.; Pan, Q.M. An Omni-Healable Supercapacitor Integrated in Dynamically Cross-Linked Polymer Networks. *Adv. Funct. Mater.* **2017**, *27*, 1700690. [CrossRef]
42. Lei, S.J.; Liu, L.; Wang, C.Y.; Shen, X.L.; Wang, C.N.; Guo, D.H.; Zeng, S.Y.; Cheng, B.C.; Xiao, Y.H.; Zhou, L. A facile in situ reduction route for preparation of spinel CoCr<sub>2</sub>O<sub>4</sub> polycrystalline nanosheets and their magnetic properties. *Crystengcomm* **2014**, *16*, 277–286. [CrossRef]
43. Guo, M.X.; Tang, B.B.; Zhang, H.M.; Yin, S.H.; Jiang, W.; Zhang, Y.M.; Li, M.Y.; Wang, H.; Jiao, L.Q. A high efficiency CoCr<sub>2</sub>O<sub>4</sub>/carbon nanotubes nanocomposite electrocatalyst for dye-sensitised solar cells. *Chem. Commun.* **2014**, *50*, 7356–7358. [CrossRef] [PubMed]
44. Rahbar-Shamskar, K.; Azar, P.A.; Rashidi, A.; Baniyaghoob, S.; Yousefi, M. Synthesis of micro/mesoporous carbon adsorbents by in-situ fast pyrolysis of reed for recovering gasoline vapor. *J. Clean. Prod.* **2020**, *259*, 120832. [CrossRef]
45. Li, W.; Liu, J.; Guo, P.F.; Li, H.Z.; Fei, B.; Guo, Y.H.; Pan, H.G.; Sun, D.L.; Fang, F.; Wu, R.B. Co/CoP Heterojunction on Hierarchically Ordered Porous Carbon as a Highly Efficient Electrocatalyst for Hydrogen and Oxygen Evolution. *Adv. Energy Mater.* **2021**, *11*, 2102134. [CrossRef]
46. Zhu, Z.J.; Yin, H.J.; Wang, Y.; Chuang, C.H.; Xing, L.; Dong, M.Y.; Lu, Y.R.; Casillas-Garcia, G.; Zheng, Y.L.; Chen, S.; et al. Coexisting Single-Atomic Fe and Ni Sites on Hierarchically Ordered Porous Carbon as a Highly Efficient ORR Electrocatalyst. *Adv. Mater.* **2020**, *32*, 2004670. [CrossRef]
47. Xiao, F.; Zhou, Y.; Zhang, H.; Wu, Y. Preparation of manganese-doped cubic carbon electrode based on ZIF-8 and its capacitive deionization performance for fluoride removal. *Sep. Purif. Technol.* **2024**, *328*, 125046. [CrossRef]
48. Meng, F.L.; Wang, Z.L.; Zhong, H.X.; Wang, J.; Yan, J.M.; Zhang, X.B. Reactive Multifunctional Template-Induced Preparation of Fe-N-Doped Mesoporous Carbon Microspheres Towards Highly Efficient Electrocatalysts for Oxygen Reduction. *Adv. Mater.* **2016**, *28*, 7948–7955. [CrossRef]
49. Al-Mamun, M.; Su, X.T.; Zhang, H.M.; Yin, H.J.; Liu, P.R.; Yang, H.G.; Wang, D.; Tang, Z.Y.; Wang, Y.; Zhao, H.J. Strongly Coupled CoCr<sub>2</sub>O<sub>4</sub>/Carbon Nanosheets as High Performance Electrocatalysts for Oxygen Evolution Reaction. *Small* **2016**, *12*, 2866–2871. [CrossRef]
50. Zhang, J.; Qian, J.; Ran, J.; Xi, P.; Yang, L.; Gao, D. Engineering Lower Coordination Atoms onto NiO/Co<sub>3</sub>O<sub>4</sub> Heterointerfaces for Boosting Oxygen Evolution Reactions. *ACS Catal.* **2020**, *10*, 12376–12384. [CrossRef]
51. Xiong, R.; Zhong, L.; Song, Y.; Xu, J.; Xiao, Y.; Cheng, B.; Lei, S. CoCr<sub>2</sub>O<sub>4</sub> Nanoparticles with Abundant Oxygen Vacancies: A New Photothermal Platform for Efficient Solar Evaporation. *ACS Mater. Lett.* **2023**, *5*, 1992–2001. [CrossRef]
52. Ding, Y.; Shi, Z.; Sun, Y.; Wu, J.; Pan, X.; Sun, J. Steering Bidirectional Sulfur Redox via Geometric/Electronic Mediator Comodulation for Li-S Batteries. *ACS Nano* **2023**, *17*, 6002–6010. [CrossRef] [PubMed]
53. Khalil, T.E.; Soliman, S.M.; Khalil, N.A.; El-Faham, A.; Foro, S.; El-Dissouky, A. Synthesis, structure, X-ray photoelectron spectroscopy (XPS), and antimicrobial, anticancer, and antioxidant activities of Co (III) complexes based on the antihypertensive hydralazine. *Appl. Organomet. Chem.* **2022**, *36*, e6565. [CrossRef]
54. Niu, Z.Q.; Liu, H.B.; Qiao, Z.L.; Qiao, K.W.; Sun, P.P.; Xu, H.X.; Wang, S.T.; Cao, D.P. Yolk-like Pt nanoparticles as cathode catalysts for low-Pt-loading proton-exchange membrane fuel cells. *Mater. Today Energy* **2022**, *27*, 101043. [CrossRef]
55. Li, W.; Wang, Y.; Xu, N.; Li, Y. High-entropy spinel oxides as efficient ORR catalysts towards enhanced kinetics for zinc-air batteries. *J. Energy Storage* **2025**, *123*, 116784. [CrossRef]

56. Chang, Q.; He, F.; Zhang, Z.; Fu, X.; Wang, Y.; Huang, C.; Li, Y. Self-Organized Integrated Electrocatalyst on Oxygen Conversion for Highly Durable Zinc-Air Batteries. *Angew. Chem. Int. Ed.* **2025**, *64*, e202416664. [[CrossRef](#)]
57. Zhang, Y.; Zhang, Z.; Jiang, G.; Mamaghani, A.H.; Sy, S.; Gao, R.; Jiang, Y.; Deng, Y.; Bai, Z.; Yang, L.; et al. Three-dimensionally ordered mesoporous  $\text{Co}_3\text{O}_4$  decorated with Mg as bifunctional oxygen electrocatalysts for high-performance zinc-air batteries. *Nano Energy* **2022**, *100*, 107425. [[CrossRef](#)]
58. Li, J.; Wan, T.; Li, J.; Zhang, Z.; Wang, Y.; Liu, G. Three-dimensionally ordered mesoporous trimetal sulfide as efficient electrocatalyst for rechargeable zinc-air batteries. *Appl. Surf. Sci.* **2022**, *575*, 151728. [[CrossRef](#)]
59. Xu, C.-X.; Zhang, J.-J.; Dou, H.-R.; Li, Y.-Z.; Li, D.-M.; Zhang, Y.-J.; Liu, B.; Inbaraj, P.; Huo, P.-P.  $\text{Fe}_4\text{N}$  particles embedded in nitrogen-doped electrospun carbon nanofibers as efficient ORR catalysts for zinc-air battery. *Rare Met.* **2025**, *44*, 3156–3169. [[CrossRef](#)]
60. Yasin, G.; Ibrahim, S.; Ibraheem, S.; Ali, S.; Iqbal, R.; Kumar, A.; Tabish, M.; Slimani, Y.; Nguyen, T.A.; Xu, H.; et al. Defective/graphitic synergy in a heteroatom-interlinked-triggered metal-free electrocatalyst for high-performance rechargeable zinc-air batteries. *J. Mater. Chem. A* **2021**, *9*, 18222–18230. [[CrossRef](#)]
61. Li, J.; Li, W.; Mi, H.; Li, Y.; Deng, L.; Zhang, Q.; He, C.; Ren, X. Bifunctional oxygen electrocatalysis on ultra-thin  $\text{Co}_9\text{S}_8/\text{MnS}$  carbon nanosheets for all-solid-state zinc-air batteries. *J. Mater. Chem. A* **2021**, *9*, 22635–22642. [[CrossRef](#)]
62. Akbarian, P.; Eshghi, A.; Asadi, A.; Kheirmand, M.  $\text{Pd}-\text{Co}_3\text{O}_4/\text{acetylene black}$  nanocomposite as an efficient and robust bifunctional ORR/OER electrocatalyst for rechargeable zinc-air batteries. *Int. J. Hydrogen Energy* **2024**, *91*, 1103–1112. [[CrossRef](#)]
63. Li, Y.; Xu, J.; Lan, F.; Wang, Y.; Jiang, H.; Wu, X.; Huang, Y.; Li, R.; Jiang, Q.; Gao, D.; et al. Breaking the Stability-Activity Trade-off of Oxygen Electrocatalyst by Gallium Bilateral-Regulation for High-Performance Zinc-Air Batteries. *Angew. Chem. Int. Ed.* **2025**, *64*, e202420481. [[CrossRef](#)] [[PubMed](#)]
64. Wu, R.; Wang, X.; Ge, L.; Zheng, Z.; Zhu, Y.; Zhou, C.; Yuan, J.; Zhu, S.; Gu, Y.; Zhou, W.; et al. N, S co-doped carbon with embedment of FeNi alloy as bifunctional oxygen electrocatalysts for rechargeable Zinc-air batteries. *Carbon* **2023**, *202*, 141–149. [[CrossRef](#)]
65. Qi, Y.; Liang, Q.; Song, K.; Zhou, X.; Liu, M.; Li, W.; Liu, F.; Jiang, Z.; Zou, X.; Chen, Z.; et al. Optimizing high-coordination shell of Co-based single-atom catalysts for efficient ORR and zinc-air batteries. *J. Energy Chem.* **2024**, *95*, 306–314. [[CrossRef](#)]
66. Liu, C.; Wu, S.; Tian, S.; Yang, J.; Li, J.; Wang, X.; Wang, L.; Chen, C.; Zhang, P.; Yang, Q. Nanoporous Fe and Co Dually Doped Carbon Nanotube-Based Oxygen Electrocatalysts for Efficient Zinc–Air Batteries. *ACS Appl. Nano Mater.* **2024**, *7*, 13536–13546. [[CrossRef](#)]
67. Cao, X.; Gao, Y.; Wang, Z.; Zeng, H.; Song, Y.; Tang, S.; Luo, L.; Gong, S.  $\text{FeNiCrCoMn}$  High-Entropy Alloy Nanoparticles Loaded on Carbon Nanotubes as Bifunctional Oxygen Catalysts for Rechargeable Zinc-Air Batteries. *ACS Appl. Mater. Interfaces* **2023**, *15*, 32365–32375. [[CrossRef](#)]
68. Allwyn, N.; Gokulnath, S.; Sathish, M. In-Situ Nanoarchitectonics of Fe/Co LDH over Cobalt-Enriched N-Doped Carbon Cookies as Facile Oxygen Redox Electrocatalysts for High-Rate Rechargeable Zinc-Air Batteries. *ACS Appl. Mater. Interfaces* **2024**, *16*, 20360–20374. [[CrossRef](#)]
69. Deng, Y.; Du, J.; Zhu, Y.; Zhao, L.; Wang, H.; Gong, Y.; Jin, J.; He, B.; Wang, R. Interface engineering of Ruddlesden-Popper perovskite/ $\text{CeO}_2$ /carbon heterojunction for rechargeable zinc-air batteries. *J. Colloid Interface Sci.* **2024**, *653*, 1775–1784. [[CrossRef](#)]
70. Zhang, J.; Li, C.; Zheng, Y.; Shen, M.; Wen, H.; Ma, R. Nickel-iron layered double hydroxides interlinked by N-doped carbon network as bifunctional electrocatalysts for rechargeable zinc-air batteries. *Diam. Relat. Mater.* **2024**, *141*, 110596. [[CrossRef](#)]
71. Wu, Q.; Gao, H.; Jiang, J.; Zhao, T.; Liu, S.; Wu, C.; Xu, G.; Zhang, L. In-situ nitrogen-doped carbon nanotube-encapsulated  $\text{Co}_9\text{S}_8$  nanoparticles as self-supporting bifunctional air electrodes for zinc-air batteries. *J. Mater. Sci. Technol.* **2025**, *222*, 1–10. [[CrossRef](#)]
72. Zhang, F.; Ji, R.; Zhu, X.; Li, H.; Wang, Y.; Wang, J.; Wang, F.; Lan, H. Strain-Regulated Pt-NiO@Ni Sub-Micron Particles Achieving Bifunctional Electrocatalysis for Zinc–Air Battery. *Small* **2023**, *19*, 2301640. [[CrossRef](#)]
73. Feng, Y.; Song, K.; Zhang, W.; Zhou, X.; Yoo, S.J.; Kim, J.-G.; Qiao, S.; Qi, Y.; Zou, X.; Chen, Z.; et al. Efficient ORR catalysts for zinc-air battery: Biomass-derived ultra-stable Co nanoparticles wrapped with graphitic layers via optimizing electron transfer. *J. Energy Chem.* **2022**, *70*, 211–218. [[CrossRef](#)]
74. Radwan, A.; Jin, H.; Liu, B.; Chen, Z.; Wu, Q.; Zhao, X.; He, D.; Mu, S. 3D-ZIF scaffold derived carbon encapsulated iron nitride as a synergistic catalyst for ORR and zinc-air battery cathodes. *Carbon* **2021**, *171*, 368–375. [[CrossRef](#)]
75. Wang, Q.; Wang, L.; Zhang, S.; Chen, Z.; Peng, W.; Li, Y.; Fan, X. MOF-on-MOF-derived  $\text{FeCo}@\text{NC}$  OER&ORR bifunctional electrocatalysts for zinc-air batteries. *J. Colloid Interface Sci.* **2025**, *677*, 800–811.